J. Fluid Mech. (2025), *vol.* 1011, A30, doi:10.1017/jfm.2025.371

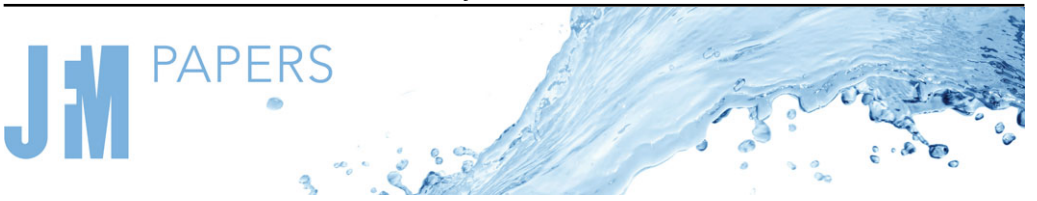

Complex-network modeling of reversal events in two-dimensional turbulent thermal convection

Rui Yang[1,2] **and Peter J. Schmid**[3]

[1]Department of Mechanical and Aerospace Engineering, Princeton University, Princeton, NJ 08544, USA

[2]Physics of Fluids Group, Max Planck Center for Complex Fluid Dynamics, J.M. Burgers Centre for Fluid Dynamics, University of Twente, Enschede 7500AE, The Netherlands

[3]Department of Mechanical Engineering, Division of Physical Sciences and Engineering (PSE), King Abdullah University of Science and Technology (KAUST), Thuwal, Saudi Arabia

Corresponding author: Rui Yang, ruiyang@princeton.edu

(Received 22 November 2024; revised 15 February 2025; accepted 22 March 2025)

Spontaneous flow reversals in buoyancy-driven flows are ubiquitous in many fields of science and engineering, often characterized by violent, intermittent occurrences. In this study, we present a complex-network-based reduced-order model to analyse intermittent events in turbulent flows, using temporal and spatial snapshot data. This framework combines elements of dynamical system theory with network science. We demonstrate its utility by applying it to data sequences from intermittent flow reversal events in two-dimensional thermal convection. This approach has proven robust in detecting and quantifying structures and predicting reversals. Additionally, it provides a perspective on the physical mechanisms underlying flow reversals through cluster evolution. This purely data-driven methodology shows the potential to enhance our understanding, prediction and control of turbulent flows and complex systems.

Key words: bénard convection

1. Introduction

Spontaneous flow reversals occur in various buoyancy-driven fluid dynamical systems (Sugiyama *et al.* 2010; Wang *et al.* 2018), such as large-scale flows in the ocean (Nunes & Norris 2006), the atmosphere (Cai *et al.* 2021), or the inner core of stars or the Earth, where such reversals are associated with the reversal of the magnetic field (Glatzmaier *et al.* 1999). They are characterized by a large range of temporal and spatial scales, high dimensionality, and intermittence. Various models, either of a stochastic nature

(Brown & Ahlers 2007, 2008) or based on simplified (nonlinear) dynamical equations (Araujo, Grossmann & Lohse 2005; Chandra & Verma 2013; Suri 2024), have been developed to account for the reversals. However, these models are mostly qualitative or often inaccurate in predicting the reversals. Progress in analysing and manipulating turbulent fluid motion is needed to better predict and control these dynamic structures. This is crucial not only for the reversals in buoyancy-driven flows but also for other problems in which the flow switches between either two competing states or a persistent state and a rare event, such as von Kármán swirling flow (de la Torre & Burguete 2007), rotating spherical Couette flow (Zimmerman, Triana & Lathrop 2011), flow mixing (Schikarski *et al.* 2019), near-wall turbulence (Jiménez & Moin 1991; Jiménez 2023), pipe flow (Avila, Barkley & Hof 2023), zonal flow bursts (von Hardenberg *et al.* 2015), Taylor–Couette turbulence (Borrero-Echeverry, Schatz & Tagg 2010) or aerodynamic bifurcation (Gayout, Bourgoin & Plihon 2021).

Data-driven modelling has advanced significantly in recent decades due to algorithmic improvements, increased data availability, and faster hardware. This approach is suitable for modelling intermittent events and is pivotal for physical insight, state estimation from limited data, prediction, control and optimization (Brunton, Noack & Koumoutsakos 2020). Typically, such modelling relies on a low-dimensional approximation of the state and system identification within that approximation. The commonly used reduced-order modelling methods include proper orthogonal decomposition (POD) (Holmes 2012; Lumey 2012), dynamic mode decomposition (DMD) (Schmid 2010) and Koopman analysis (Mezić 2013; Giannakis *et al.* 2018), which can reduce computational costs and extract the dominant flow patterns effectively, and has been applied broadly (Kutz *et al.* 2016; Kou & Zhang 2017; Kou, Le Clainche & Zhang 2018; Schmid 2022; Yang *et al.* 2022). For Rayleigh–Bénard convection, Podvin and Sergent use POD modes to comprehensively investigate the large-scale circulation (LSC) and the reversal dynamics (Podvin & Sergent 2012, 2015, 2017; Castillo-Castellanos *et al.* 2019; Soucasse *et al.* 2019) in two- and three-dimensional turbulent convection. Xu, Chen & Xi (2021) use POD modes to study the reversal dynamics in two-dimensional circular convection cells, and compare them with the Fourier modes. Chandra & Verma (2011) use large-scale Fourier modes, coupled with symmetry transformations, to identify the dynamics of flow reversals.

Recent developments in data-driven modelling include the sparse identification of nonlinear dynamics (SINDy) algorithm, which identifies accurate parsimonious models from data (Brunton, Proctor & Kutz 2016) but is challenging to scale to large-scale problems due to the size of the associated feature spaces; in addition, we have, among many other models, access to neural network models (Vlachas *et al.* 2018) that avoid high computational cost but have limited interpretability and provide little physical insights. An alternative paradigm based on cluster modelling has recently been applied to fluid flows, as it presents a promising course of action for understanding the physics behind complex fluid motions (Kaiser *et al.* 2014; Fernex, Noack & Semaan 2021; Deng *et al.* 2022; Hou, Deng & Noack 2024), including large-scale flow structures in three-dimensional Rayleigh–Bénard convection (Maity *et al.* 2022, 2023), flow past cylinder wakes (Deng *et al.* 2022; Hou *et al.* 2024), and Lagrangian vortex dynamics (Hadjighasem *et al.* 2016).

In this work, we promote an alternative cluster modelling technique based on a complex network, which explicitly considers the topology of the network and is designed to handle directionality in the patterns of connecting edges between nodes. The main goal of this approach is to leverage a cluster-based framework for better understanding, predicting and potentially controlling intricate flow behaviour. As a model system, we concentrate on two-dimensional turbulent Rayleigh–Bénard convection (Ahlers, Grossmann & Lohse 2009; Lohse & Xia 2010; Shishkina 2021; Lohse & Shishkina 2024), consisting of a fluid

layer heated from below and cooled from above, where intermittent flow reversals are readily observed (Sugiyama *et al.* 2010; Chandra & Verma 2013). Starting with a time-resolved snapshot sequence of a trajectory in a high-dimensional phase space spanned by appropriate coherent flow fields (given by e.g. POD modes), the thus reduced-order phase space is discretized, and the resulting trajectory is converted into a Markov matrix describing the transition probabilities between various phase-space elements over one time step. This Markov matrix is subsequently interpreted as a directed, weighted graph (Chartrand & Zhang 2013) consisting of all occupied phase-space elements, encoding the dynamics of the data sequence probabilistically. Different from a K-means clustering algorithm used in previous cluster-based models (Kaiser *et al.* 2014; Fernex *et al.* 2021; Hou *et al.* 2024), we reorganize the original network into larger communities, defined as groups of nodes with strong intraconnectivity and weak interconnectivity, to isolate persistent motion from rare outlier events (Newman 2006; Leicht & Newman 2008; Schmid *et al.* 2018). This clustering method has proven itself effective in classifying communities, and makes use of the information contained in the edges, i.e. the links between nodes. An explicit network model of the flow reversals is obtained, which effectively categorizes and predicts the intermittent reversal events. Each of the procedural steps will be further explained in detail.

The organization of the paper is as follows. § 2 introduces the flow configuration, including the direct numerical simulations of thermal convection, together with the control and response parameters. § 3 introduces details of the complex-network model and presents results. Conclusions are offered in § 4.

2. Flow configuration

Direct numerical simulations (DNS) for incompressible Oberbeck–Boussinesq flow are performed (Verzicco & Orlandi 1996), which have been widely used to study thermal convection (Yang *et al.* 2016, 2020; Blass *et al.* 2020). The non-dimensionalized governing equations, including the incompressibility condition, are given by

$$\partial_t u_i + u_j\, \partial_j u_i = -\partial_i p + \sqrt{\frac{Pr}{Ra}}\, \partial_j \partial_j u_i + T\delta_{iz}, \tag{2.1}$$

$$\partial_t T + u_i\, \partial_i T = \frac{1}{\sqrt{Ra\, Pr}}\, \partial_j \partial_j T, \tag{2.2}$$

$$\partial_i u_i = 0, \tag{2.3}$$

where u, T and p are the dimensionless velocity, temperature and pressure. The dimensionless control parameters include the Rayleigh number $Ra = \alpha g H^3 \Delta/(\nu\kappa)$, the Prandtl number $Pr = \nu/\kappa$, and the aspect ratio of the container Γ, where α, ν and κ denote the thermal expansion coefficient, the kinematic viscosity and the thermal diffusivity of the fluid, respectively. The parameter g denotes the gravitational acceleration, and Δ stands for the temperature difference between the bottom and top boundaries. The time, lengths and temperature are rendered dimensionless by the free-fall time $t_f = \sqrt{H/(\alpha g \Delta)}$, the free-fall velocity $U = \sqrt{\alpha g \Delta H}$, the height H of the container, and the temperature difference Δ, respectively. The simulations are conducted in a two-dimensional square box with no-slip and impermeable boundary conditions for all walls. The governing equations in a Cartesian geometry were solved by a second-order finite-difference scheme in space and by a fractional-step third-order Runge–Kutta scheme combined with the Crank–Nicolson scheme for the implicit terms in time (Verzicco & Orlandi 1996).

Ra	Pr	t_{total}	Grid
10^6	4.3	10 000	72×72
1×10^8 (model)	4.3	10 000	288×288
1×10^8 (test)	4.3	10 000	288×288
2×10^8	4.3	10 000	288×288
10^7	3	10 000	144×144
10^7	4.3	10 000	144×144
10^7	10	10 000	144×144

Table 1. Simulation parameters and grid information. The columns from left to right indicate the Rayleigh number Ra , the Prandtl number Pr, the total simulation time t_{total} in free-fall time units, and the grid information.

Reversals can be detected by the volume-averaged angular momentum about the centre of the box L, which is defined as

$$L(t) = \langle -(z - H/2)\, u(x, t) + (x - H/2)\, v(x, t) \rangle_V \,, \tag{2.4}$$

where u, v are the horizontal and vertical velocities, respectively. Statistics were collected after a sufficiently long start-up to ensure that the flow had reached a quasi-statistical stationary state. Here, we restrict ourselves to the study of flow reversals in a two-dimensional square geometry ($\Gamma = 1$) and span the parameter ranges $10^6 \leq Ra \leq 2 \times 10^8$, $3 \leq Pr \leq 10$. The numerical details of the simulations are listed in table 1. We choose $Ra = 10^8$ and $Pr = 4.3$ as the default case, unless otherwise specified. Typical flow structures with a domain-size LSC are shown in figure 1(a) from one simulation but at different time instants. The flow reversal is indicated by the arrow directions.

3. Complex-network modelling and results

3.1. *Dimensionality reduction by phase-space embedding*

The first step in our approach is to project the original dataset onto a lower-dimensional space, which is an optional process but significantly reduces the overall computational costs. We choose the POD modes (Holmes 2012; Lumey 2012) as a convenient starting point. The output frequency of the temperature and velocity fields is linked to one free-fall time unit. This choice ensures that we have sufficient data points to capture the transient reversal process. Selecting a time step that is too large would result in a loss of information regarding the transition, and could compromise the quality of the clustering analysis. By downsampling and projecting the original flow fields (consisting of temperature T and velocity u, v fields collected into a composite data matrix; see figure 1b) onto the retained POD modes, we obtain a time series for the expansion coefficients.

Figure 1(c) shows the magnitude of POD modes, in descending order and numbered by k. The first mode ($k = 0$) is the steady mode representing the mean field, and the following two modes, M_1 and M_2, are the dominant modes contributing to the flow reversal. Figure 1(d) shows the time series of L, M_1 and M_2. Surprisingly, the reconstructed angular momentum L', based on M_1 and M_2 only, can well reproduce the original L, indicating that it suffices to consider only the first two POD modes, beyond the mean flow mode. More details on other POD modes are described in Appendix A. From the temporal evolution of L, one can clearly detect the random and intermittent occurrence of reversals of the LSC orientation. Such reversal events have been found to obey a

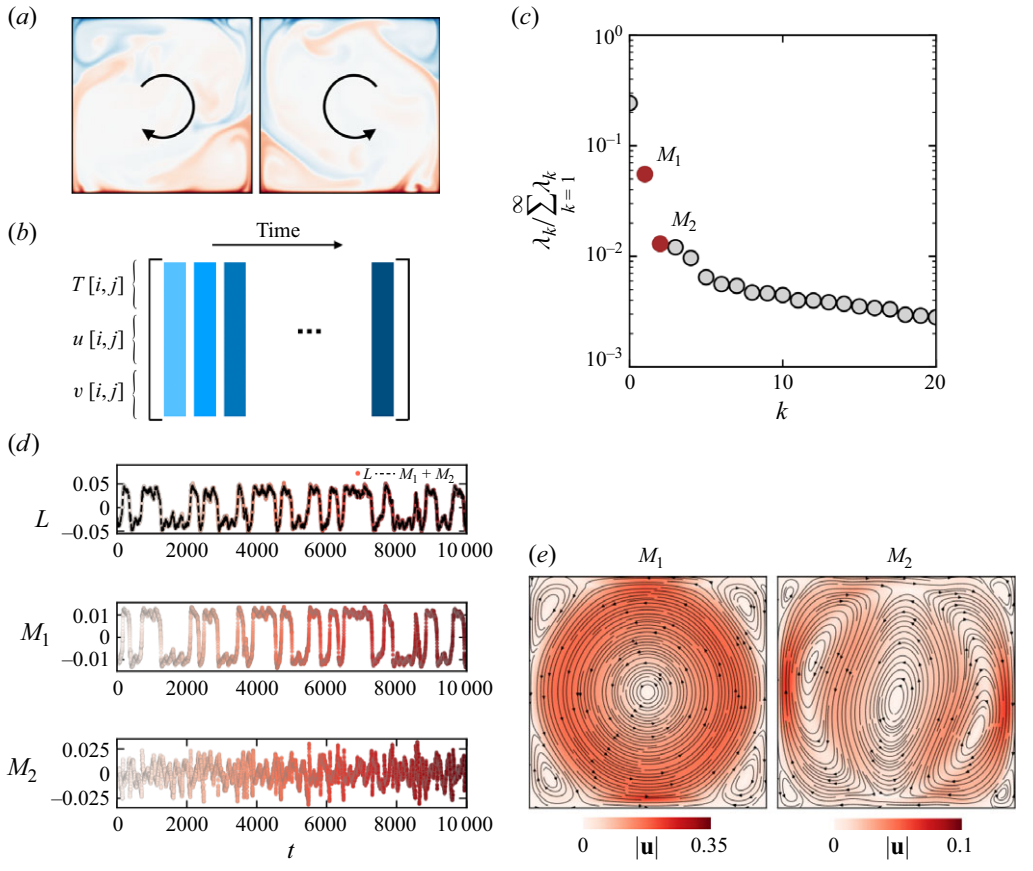

Figure 1. Sketch of the clustering procedure. (*a*) Temperature fields from the original data; two snapshots show different LSC orientations. (*b*) Data collection and reorganization into a matrix, including the state variables T, u and v. (*c*) The normalized magnitude of POD modes in descending order k. Here, M_1 and M_2 represent the first two dominant modes after the steady mode at $k = 0$. (*d*) The time series of the value of L and the first two POD modes M_1 and M_2. The dashed line in the plot of L represents the reconstructed L' from M_1 and M_2. (*e*) The reconstructed velocity magnitude field based on M_1 and M_2; the velocity direction is shown by streamlines.

Poisson process, i.e. successive reversal events are independent of each other (see Xi & Xia 2007).

Figure 1(*e*) shows the reconstructed flow field based on M_1 and M_2, where M_1 stands for the single-roll structure with the changing of sign representing the flow reversal, and M_2 corresponds to the three-roll flow structure. The two-dimensional phase space of M_1 and M_2 is displayed in figure 2(*a*). We observe two distinct regions representing stable LSCs with different directions, and the centre region capturing the transitions between the two stable LSCs. We also checked that higher-order phase-space modes describe noisy signals and do not contribute additional information beyond the two retained modes. A video of the temporal evolution process of the POD phase space can be found in the supplementary material (available at https://doi.org/10.1017/jfm.2025.371).

3.2. *Constructing the Markov matrix*

Following the phase-space trajectory in the lower-dimensional representation of the flow reversal, we proceed by discretizing the phase space to estimate transition probabilities.

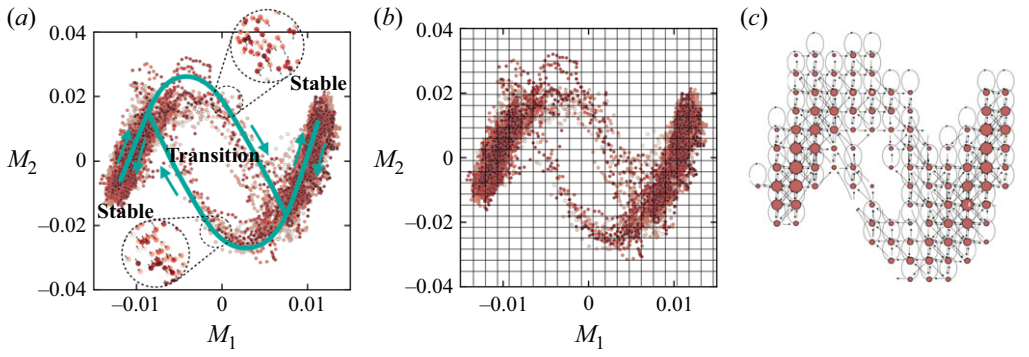

Figure 2. (*a*) Phase space spanned by the two dominant POD coefficients M_1 and M_2, each point representing one instant in time. The cyan lines show the direction of the motion. (*b*) An illustration of the discretized network of the phase space from (*a*). (*c*) The final complex network based on (3.3) with $N = 30$. The circles represent nodes, with the size indicating the density. The arrows represent the edges.

A straightforward and efficient discretization uses rectangular boxes (more generally hypercubes for phase spaces of any dimension) and a counting measure. More formally, we denote the set of box elements from our discretization by $\{B_1, \ldots, B_N\}$, where N denotes the number of boxes, and write the indicator function for B_i as

$$\mathbb{I}_{B_i(x)} = \begin{cases} 1, & \text{if } x \in B_i, \\ 0, & \text{otherwise.} \end{cases} \tag{3.1}$$

We further introduce a suitable density measure $m(B_i)$ for each box B_i, which we take as the number of instances (phase-space points) that it contains, and a continuous operator $\mathcal{P}$ that describes the transition probabilities between phase-space elements. A Galerkin projection of $\mathcal{P}$ onto a subspace spanned by the indicator function is expressed by

$$\int \mathbb{I}_{\mathrm{B}_j} \mathcal{P}\ \mathbb{I}_{\mathrm{B}_i}\, \mathrm{d}m = m\left(B_i \cap \mathcal{F}^{-1}\left(B_j\right)\right). \tag{3.2}$$

The resulting transition probability matrix P can be defined by its elements according to

$$P_{ij} = \frac{m\left(B_i \cap \mathcal{F}^{-1}\left(B_j\right)\right)}{m\left(B_i\right)}, \quad i, j = 1, \ldots, N, \tag{3.3}$$

where $\mathcal{F}^{-1}$ denotes the temporal backstep operator, i.e. we evaluate its argument at the previous time step, which is identical to the original data interval for a time-discrete formulation. The numerator in (3.3) represents the number of transitions into box B_i from box B_j over a single time step, while the denominator denotes the total number of states located within the box B_i. The ratio approximates the Markov transition probability between boxes B_j and B_i. The complete matrix P furnishes an approximation of the Markov transition probability matrix for all boxes in our phase-space discretization. Our particular discretization is referred to as the Ulam–Galerkin method (Ulam 1960; Li 1976; Kaiser *et al.* 2014). Mathematically, this matrix P constitutes a finite-dimensional approximation of the Frobenius–Perron operator – the adjoint of the Koopman operator (Lasota & Mackey 2013; Kaiser *et al.* 2014). The above approximation of the Frobenius–Perron operator can be thought of as the analogue of the DMD matrix for approximating the Koopman operator.

We use a discretization with 24 boxes in each direction, which yields 257 cells in total; see the illustration in figure 2(*b*). The result of the discretized phase space is shown in figure 2(*c*): the circles represent nodes in the network, with the size indicating local measure density, and the arrows represent the edges indicating the cell-to-cell transitions. The network reveals two stable regions characterized by larger nodes. Before proceeding with our analysis, it is important to note that the resolution of the phase-space discretization remains an adjustable parameter in our study. A low-resolution discretization leads to too few communities and may lose pertinent information about the transition regions. A high-resolution discretization, on the other hand, identifies too many independent communities and noisy signals, since the data points that fall inside the control volumes are far too sparse. A more detailed discussion of balancing these two extreme cases is included in the Appendix B. For our case, we choose a proper resolution of the phase-space trajectory that yields a suitable number of communities.

3.3. *Community clustering*

To regroup the network into coherent clusters, we define a community as a collection of nodes that exhibits strong intraconnectivity (within the community) but weak interconnectivity (to other communities). Several algorithms are available for detecting graph communities within large networks, many of which use a measure of interconnectivity referred to as modularity (Newman 2006; Leicht & Newman 2008; Schmid *et al.* 2018) and defined as

$$Q = \frac{1}{N}\sum_{i,j}\left[P_{ij} - \frac{k_i^{in}k_j^{out}}{N}\right]\delta_{c_i,c_j} \tag{3.4}$$

where $k_i^{in,out}$ represents the in-degree (the number of edges that point into the node) or out-degree (the number of edges that point out from the node) of the ith node, and c_i denotes the ith community. The Kronecker symbol is represented by $\delta_{i,j}$. Based on this definition, we seek a partition of the graph into communities c_i such that Q attains a maximum value. To this end, we employ a modularity-based approximation algorithm (Leicht & Newman 2008), which incrementally improves the modularity Q by exploiting the spectral properties of the graph; it is computationally efficient, and produces good and robust results in practice (Danon *et al.* 2005; Leicht & Newman 2008).

Starting with a simplified configuration with only two communities, we define s_i to be $+1$ when i is in the first community, and -1 if it is in the second community. Then δ_{c_i,c_j} can be represented by $1/2(s_i s_j + 1)$, and (3.4) can be rewritten as

$$Q = \frac{1}{2m}\sum_{ij}\left[A_{ij} - \frac{k_i^{in}k_j^{out}}{m}\right](s_i s_j + 1) = \frac{1}{4m}\mathbf{s}^T(\mathbf{B} + \mathbf{B}^T)\mathbf{s}, \tag{3.5}$$

where $\mathbf{s}$ is the vector form of s_i, and $\mathbf{B}$ is the so-called modularity matrix, whose entries are defined as

$$B_{ij} = A_{ij} - \frac{k_i^{in}k_j^{out}}{m}. \tag{3.6}$$

The goal is then to find the vector $\boldsymbol{s}$ that maximizes Q for a given $\mathbf{B}$. In the algorithm, the eigenvector corresponding to the largest positive eigenvalue of the symmetric matrix $\mathbf{B} + \mathbf{B}^{\mathrm{T}}$ is calculated, after which communities are assigned based on the signs of the elements of this eigenvector. The reasoning behind this procedural step is the goal to align $\boldsymbol{s}$ maximally parallel to the leading eigenvector of $\mathbf{B} + \mathbf{B}^{\mathrm{T}}$ (Leicht & Newman 2008).

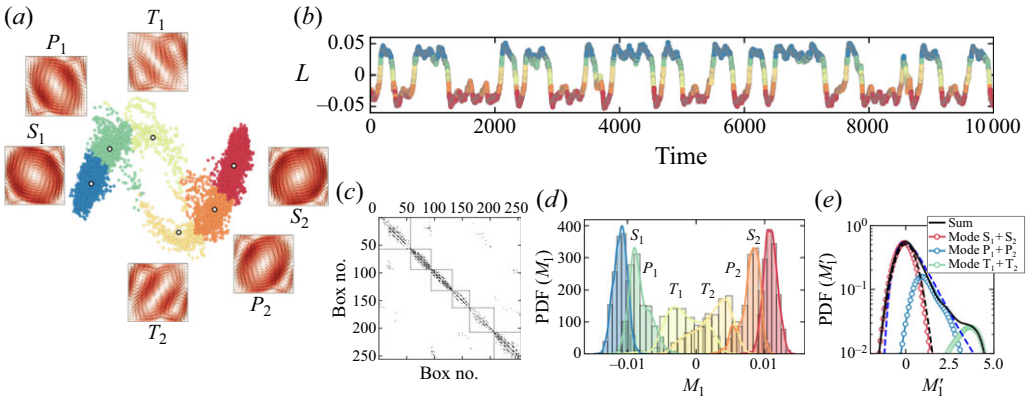

Figure 3. (*a*) The phase space of M_1 and M_2, with colours representing different communities, identified based on (3.4). The symbols mark the centroids of each community, and the snapshots show the averaged velocity magnitudes field in the communities. (*b*) The time series of L, with the colours representing different communities. (*c*) Fill pattern of the transition probability matrix after applying the clustering algorithm, displaying six distinct communities. (*d*) Separated PDF of M_1 for each community. (*e*) The PDF of M_1' for composite symmetric modes. The dashed lines represent Gaussian distributions and the extreme value distribution (Wang *et al.* 2018).

Scaling to more than two communities, we follow a simple course: we first divide the network into two communities, then subdivide those communities, and so on, until we reach a point where further divisions no longer increase Q. A more detailed description of the clustering process can be found in Newman (2006) and Leicht & Newman (2008).

By applying community clustering on the POD-reduced data of flow reversals, we obtained six distinct communities, as depicted in figure 3(*a*), along with the centroid-averaged flow field for each community. These communities include (i) two stable communities (S_1, S_2) where the LSC dominates and the flow state is stable, (ii) two precursor communities (P_1, P_2) where the LSC is weaker but nonetheless sustained, and (iii) two transition communities (T_1, T_2) where the LSC breaks down and the flow-state switches from one direction to the opposite. The precursor community is named based on the fact that the trajectory must pass through P_1 or P_2 in a reversal event. Consequently, the transition from P_1 (P_2) to T_1 (T_2) carries information that signals the initiation of a reversal. In our following predictions, we also use this precursor information as the start of a reversal. Our method explicitly accounts for the network's topology and is particularly suited to handle directionality in the patterns of edges between nodes, which the K-means algorithm neglects. To further illustrate this difference, we provide a comparison of results from a K-means clustering method and from our modularity-based method in Appendix C.

Figure 3(*b*) shows the time series of L, with different colours representing different communities. By retaining the identities of the original snapshots within each community, we reorganize the original transition probability matrix P into a block diagonal form. The dense blocks on the diagonal describe motion within each community, while the sparse off-diagonal blocks represent transitions between communities. The fill pattern of the 257×257 transition matrix, shown in figure 3(*c*), highlights the six diagonal blocks representing the distinct communities. The fill pattern represents the presence or absence of edges between nodes in a graph, and helps us to visualize the connectivity of the graph. A non-zero entry (black points in figure 3*c*) at position (i, j) indicates an edge between nodes i and j, while a zero indicates no link. The dashed boxes represent the identified communities based on (3.4). The on-diagonal points indicate that the state stays

in the same node, the near-diagonal points within each box show a strong connectivity among different nodes in the same community, and the sparse points outside boxes indicate connections between different communities, including precursor and transition states. These precursor structures could be targeted for effective control efforts to prevent reversals, thereby maintaining the system in a single direction of LSC.

We further analyse the probability distribution of M_1 for each community in figure 3(*d*). Stable communities exhibit a steeper curve and shorter tail, while transition communities show a much broader distribution. Combining the symmetric communities, we plot the probability density function (PDF) in figure 3(*e*), which shows that the stable communities follow a Gaussian distribution, whereas the precursor communities contribute to the long tail of the extreme value distribution. This behaviour can be well described by the generalized extreme-value distribution function (Lucarini *et al.* 2016; Wang *et al.* 2018)

$$\mathrm{PDF}(M_1') = \frac{1}{\beta}(1+\chi M_1')^{-(1/\chi+1)}\,\mathrm{e}^{-(1+\chi M_1')^{-1/\chi}}, \tag{3.7}$$

where $M_1' = (M_1-\mu)/\beta$, the variable χ denotes the shape parameter, set to $\chi = 0.1$, and $\mu(\chi)$ and $\beta(\chi)$ are both functions of χ (for details, see Lucarini *et al.* 2016; Wang *et al.* 2018). This distribution aligns with the previous observations of the reversal statistics (Wang *et al.* 2018), and the classification successfully delineates the precursor and transition states from the stable states – another demonstration of the effectiveness of the cluster model.

3.4. *Prediction based on the Markov matrix*

Given that the Markov matrix describes the probabilities of transition between various phase-space elements over one time step, it can be used to predict flow reversals by calculating the transition probability for subsequent time steps as follows:

$$\boldsymbol{a}_{t+1,i} = \begin{cases} 1, & \text{if } \boldsymbol{a}_t P \text{ is max at } i, \\ 0, & \text{otherwise.} \end{cases} \tag{3.8}$$

Here, $\boldsymbol{a}$ is the state vector with unity at the current state, and zeros at all other states, and the index ranges from $i = 1$ to $i = 257$, which covers the total number of possible states (nodes). The next state is determined by the transition route with the highest probability among all possible paths, given an initial state with $x_0 = [0, 0, \ldots, 1, 0, \ldots, 0]$, where the location of the coefficient 1 represents the location of the initial state. We compute the next state using the Markov matrix to obtain the probability vector $[P_1, P_2, \ldots, P_N]$. This vector represents the probability of the state location at the next step. We then update the state by selecting the location with the highest probability in the vector, e.g. P_i, and then reset the state as $x_1 = [0, 0, \ldots, 1, 0, \ldots, 0]$, where 1 is located at i. This updated state is then used for subsequent calculations.

Using this approach, the state traverses the phase space. We first build the cluster model (Markov matrix) using a test dataset with 10 000 snapshots, then apply this model to a new dataset with another 10 000 snapshots. If we rely solely on the above method, then the state will eventually converge to the stable communities (which are always characterized by the highest probabilities). This results in the model's failure to capture rare reversal states. To overcome this limitation, we introduce a simple correction to the state before the reversal starts, denoted as t_{corr}. The correction scheme adjusts the predicted state from the stable community to the actual state near the transition community in phase space at t_{corr}. After this correction, the state evolves again following the Markov matrix (as described in (3.8)), until it once more reaches the next reversal. We define t_{tran} as the time when the actual

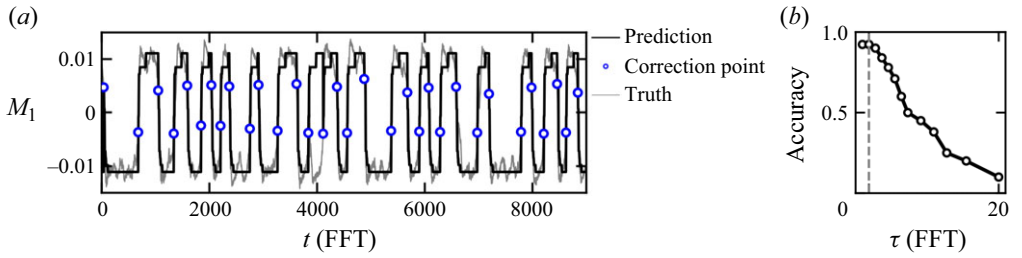

Figure 4. Test of the predictability of the cluster model. (*a*) The grey line shows the time series of M_1 for the test dataset, and the black line shows the prediction based on the Markov matrix and (3.8). The blue symbols represent the locations when a correction is added. (*b*) The accuracy of prediction as a function of the shift time τ.

state is in a precursor community and is moving to a transition community at the next step. To assess the effect of the corrective time t_{corr} relative to t_{tran}, we introduce the shift time $\tau = t_{tran} - t_{corr}$. A value $\tau = 0$ implies that the correction is applied right when the state switches to the transition community at the next step. The prediction accuracy (or, more specifically, the fraction of successful predictions; Farazmand & Sapsis 2017; Vela-Martín & Avila 2024) is defined as N_m/N_t, where N_m denotes the number of correctly matched reversal events between the actual reversal of mode M_1 and the predicted reversal, which is determined by the change in sign of M_1; the denominator N_t represents the total number of predicted reversals.

The prediction results, shown in figure 4(*a*), demonstrate that the cluster model accurately captures the reversals even for the new (unseen) data. Further analysis reveals that the prediction accuracy peaks at approximately 92 % when using t_{tran} for corrections – and starts to decrease if the correction is applied earlier than t_{tran}, as shown in figure 4(*b*). High prediction accuracy is achieved primarily when the system is near a transition point ($\tau \to 0$). This is due to strong fluctuations in the $L(t)$ evolution curve. Occasionally, L exhibits a drop without leading to a subsequent transition, which complicates the identification of real reversals. As a result, the prediction accuracy tends to diminish when attempting to predict upstream of a transition. Nonetheless, we found that t_{tran} is a good indicator and provides useful insight into how far in advance of a transition an accurate prediction of a reversal process is possible. We also compared the prediction of reversals from our model and from a simple threshold-based approach that uses an arbitrary value of $|L|$ (see Appendix D). The results demonstrate that the identified community structure provides a basis for a meaningful prediction of likely reversals, which can potentially be used for effective control strategies for the reversal processes (Zhang *et al.* 2020; Zhao *et al.* 2022; Guo *et al.* 2023).

3.5. *Extension to different Ra and Pr values*

Finally, we extend our analysis to different values of Ra and Pr. The identified communities are shown in figure 5. From the cluster pattern, one can also gain insight into the dependence of flow reversals on Ra and Pr, in combination with the flow strength shown in figure 6. At low Ra, the flow reversal occurs periodically, and the cluster becomes well mixed without distinct branches; see figure 5(*a*). As Ra increases, the two stable regions increasingly separate, making transitions between the two different stable communities more difficult, as shown in figure 5(*b*). This separation continues until the Rayleigh number Ra exceeds a critical value (e.g. $Ra > 2 \times 10^8$ at $Pr = 4.3$), at which point the LSC is sufficiently strong (see the increasing flow strength as Ra increases in

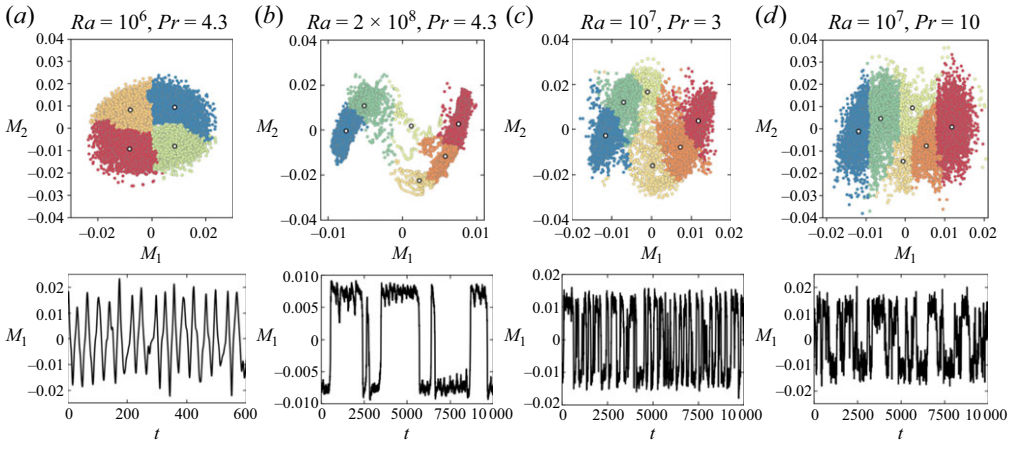

Figure 5. The two-dimensional phase space for different values of Ra and Pr, with the colours representing the communities identified based on (3.4), and the corresponding time series of the dominant mode M_1.

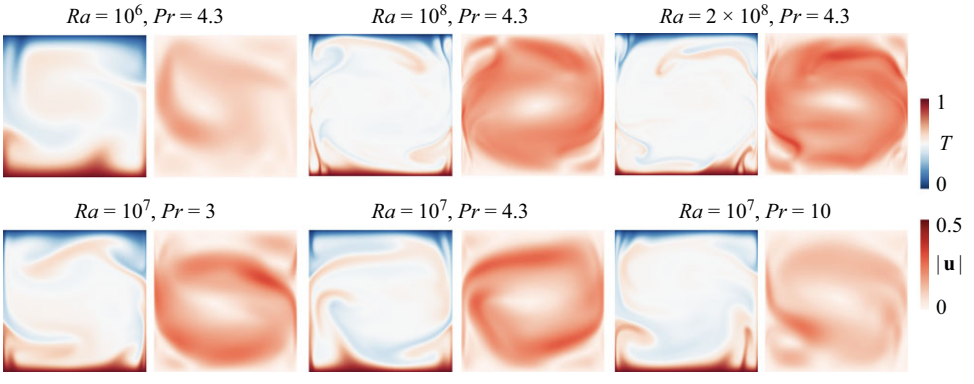

Figure 6. Snapshots of the temperature and flow strength fields for different Ra and Pr values.

figure 6) and flow reversals cease to occur. At both low and high Prandtl numbers Pr, the two stable communities in the cluster pattern are not well separated, as shown in figures 5(*c*,*d*). This situation corresponds to a weaker LSC (see the flow strength in figure 6 at $Pr = 10$), which is due to chaotic plume emission that impedes the establishment of a stable LSC (Li *et al.* 2021). Consequently, flow reversals disappear at higher Ra due to a strong LSC, which suppresses the reversal, while they also diminish at low and high Prandtl numbers owing to a weak LSC.

Note that the mode M_1 is always the first dominant mode, while M_2 is selected based on the cluster structures for different Ra and Pr, and the order may change due to the chaotic nature of the underlying flow; see more details in Appendix A. In previous work by Castillo-Castellanos *et al.* (2019), the cluster pattern was also explored for different Ra. While our cluster patterns differ from theirs due to a different selection of POD modes, the observed and reported tendency of cluster evolution with varying Ra shows similarities: for low Ra ($\sim 10^6$), the cluster shrinks and is better mixed without a distinct branch, since the reversal becomes increasingly periodic, while for high Ra ($> 2 \times 10^8$), only one branch emerges as the reversal event disappears.

4. Conclusions

In conclusion, we have presented a purely data-driven cluster-based approach utilizing set-theoretic tools and cluster analysis to examine reversal events in turbulent thermal convection. This method effectively represents the temporal evolution of the primary flow dynamics, including cluster identification and probability distributions for the system behaviour. The network-based model clearly identifies three types of key communities: the stable communities, where the large-scale circulation (LSC) maintains a consistent orientation; the transition communities, where the LSC is changing orientation, and the precursor community, where the LSC is stable but near transition, which is crucial for early prediction of reversal events. The cluster model is also capable of predicting flow reversals, using the cluster community information and the Markov matrix. We quantify the dependence of the prediction accuracy for the reversal events as a function of τ: for predictions later in the transition state, the results are very encouraging and accurate, whereas for predictions from the earlier stable state, we obtain results based on the ergodic probability. Additionally, the model's cluster pattern offers insight into the mechanism of flow reversal within the (Ra, Pr) parameter space. Specifically, reversals are suppressed at large Rayleigh numbers due to the presence of a strong LSC (represented by M_1), reflected in the separation of stable communities in the cluster pattern. At high and low Pr and low Ra, on the other hand, the cluster pattern shows a mixing of states without distinct and well-separated communities due to chaotic plume emissions, and hence a weaker LSC.

It is important to note that we use only two POD modes for the cluster analysis since they appear sufficient to capture the reversal event and angular momentum dynamics. Nevertheless, we emphasize that this cluster-based modelling framework can readily be applied to high-dimensional systems, as demonstrated in recent work (Giorgini, Souza & Schmid 2024); the cluster dynamics and reversal study in higher-dimensional systems deserves further exploration in a future effort.

Finally, this purely data-driven approach can be extended to other flow systems that switch between co-existing states or between persistent dynamics and rare events; examples, among many others, include bursts in zonal flows (von Hardenberg *et al.* 2015), near-wall turbulence (Jiménez & Moin 1991; Jiménez 2023), buoyancy-driven phase-change flows (Yang *et al.* 2023; Du, Calzavarini & Sun 2024), and pipe flows (Avila *et al.* 2023). Furthermore, potential applications in control-oriented extensions (Wang, Zhou & Sun 2020; Yang *et al.* 2020; Zhang *et al.* 2020; Zhao *et al.* 2022, 2024) could broaden its utility across various complex dynamical phenomena.

Supplementary movie. Supplementary movie is available at https://doi.org/10.1017/jfm.2025.371.

Acknowledgements. R.Y. would like to thank Professor D. Lohse and Professor A. Prosperetti for their helpful discussions and deep insights.

Funding. This research was supported by the 2022 Geophysical Fluid Dynamics Summer Fellowship at the Woods Hole Oceanographic Institution. R.Y. was also supported by the EuroHPC Joint Undertaking for awarding the projects EHPC-REG2022R03-208 and EHPC-REG-2023R03-178 for access to the EuroHPC supercomputer Discoverer. This work was also financially supported by the European Union (ERC, MultiMelt, 101094492).

Declaration of interests. The authors report no conflict of interest.

Appendix A. Proper orthogonal decomposition details

For high-dimensional data such as turbulent flow fields, data compression with lossless POD can reduce the computational cost of clustering by decomposing the data field $\mathbf{X}$ into

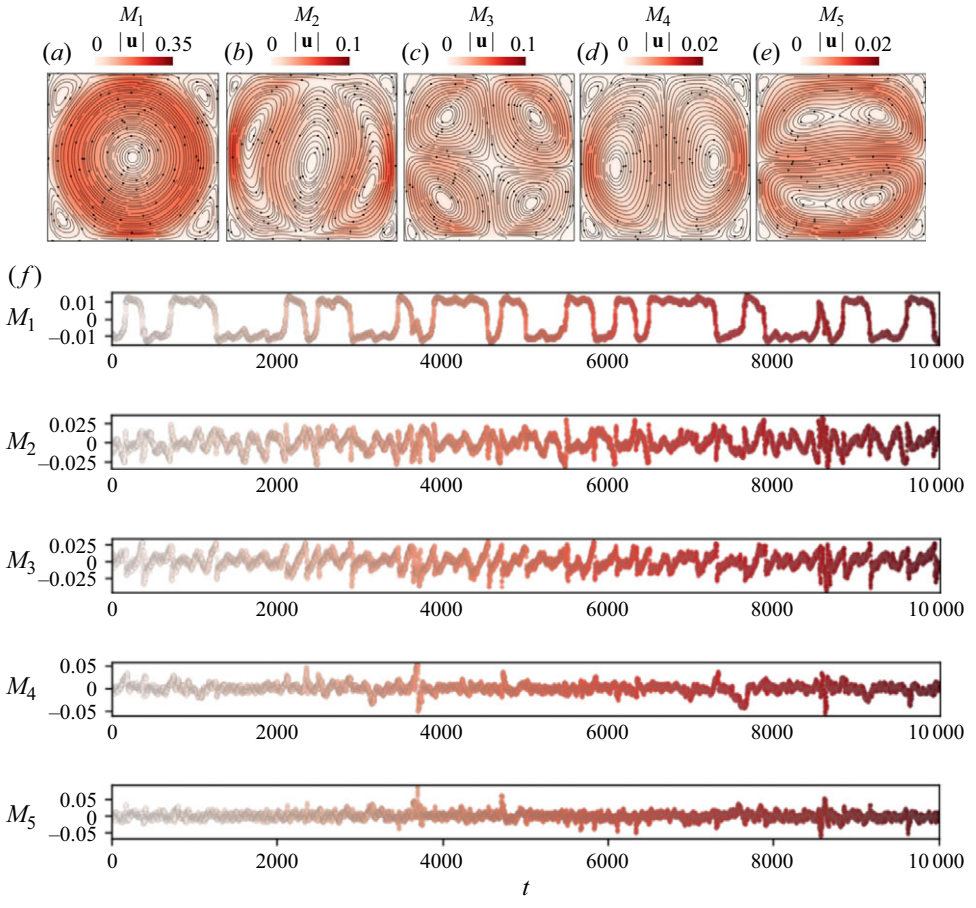

Figure 7. (*a–e*) The reconstructed velocity field, based on each of the first five POD modes for $Ra = 10^8$, $Pr = 4.3$, with the colours representing the magnitude of the flow velocity, and the streamlines representing the direction of the flow. (*f*) The time series of the value of each POD mode.

a set of POD modes according to

$$X(n, t) = \sum_{k=1}^{\infty} a_k(t)\, \phi_k(n), \tag{A1}$$

where $\phi_k(n)$ is a deterministic spatial function, and $a_k(t)$ is the corresponding temporal coefficient.

First, we reorganize the multidimensional data $(T, u_x, u_z)_{ij}$ in each snapshot into a corresponding one-dimensional real vector. At this stage we also downsample in space to further reduce the computational load (Yang *et al.* 2022). The time series can then be represented by an ordered sequence $\mathbf{X} = \mathbf{x}_n, \ \ n = 1, \ldots, N$, where N represents the number of snapshots. We next decompose $\mathbf{X}$ using a singular value decomposition according to $\mathbf{X} = \mathbf{U}\Sigma\mathbf{V}^*$, where $\mathbf{U}$ contains the spatial structures $\phi_k(n)$, Σ contains the magnitudes of each mode, and $\mathbf{V}^*$ contains the temporal coefficients $a_k(t)$.

For example, the reconstructed flow structures based on each of the first five POD modes for $Ra = 10^8, \ \ Pr = 4.3$ are shown in figure 7. Each of them shows a characteristic flow pattern, related to the LSC. In figure 8, we display the two-dimensional phase spaces

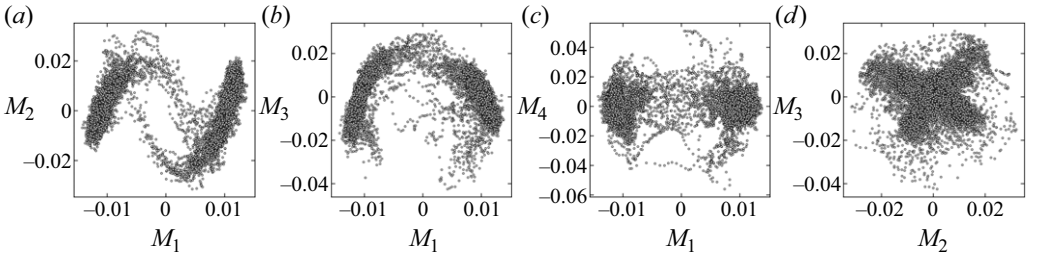

Figure 8. Two-dimensional phase spaces of (*a*) (M_1, M_2), (*b*) (M_1, M_3), (*c*) (M_1, M_4), (*d*) (M_2, M_3).

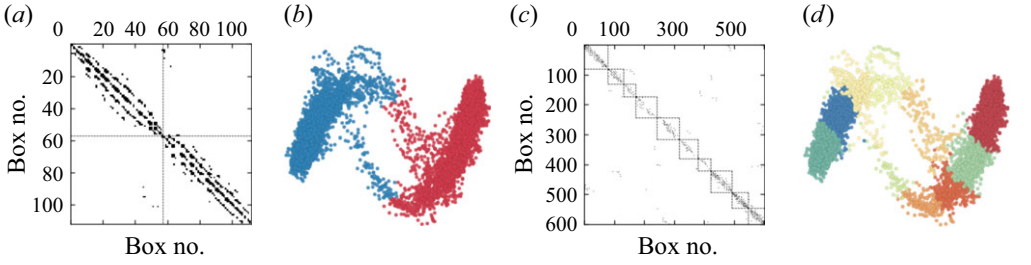

Figure 9. (*a*) Fill pattern of the transition probability matrix after the clustering algorithm with box number 15 in both directions, consisting of 112 cells in total, and displaying two communities. (*b*) The corresponding phase space of M_1 and M_2, with the colours representing different clusters. (*c*) Fill pattern of the transition probability matrix after the clustering algorithm with box number 40 in both directions, consisting of 601 cells in total, and displaying ten communities. (*d*) The corresponding phase space of M_1 and M_2, with the colours representing different clusters.

of different combinations of POD modes; from this figure, we conclude that only the (M_1, M_2) phase space captures both stable states as well as distinct transition states. The dominant modes are similar to those reported in Podvin & Sergent (2015), albeit in different order – a feature attributable to a different Ra or the chaotic nature of the underlying flow.

Appendix B. The discretization resolution effect on the cluster modelling

The discretization of phase space is marked by crucial adjustable parameters in our analysis. It must be sufficiently fine to accurately approximate the phase-space trajectory, and at the same time sufficiently coarse to contain enough trajectory points for a precise representation of the transition probabilities. To demonstrate the impact of the discretization box size, we compare results using 15 boxes in both directions (low resolution), and 40 boxes in both directions (high resolution). As shown in figure 9, a low-resolution discretization (figures 9*a*,*b*) leads to the clusters being divided into two communities, losing detailed information about the precursor and transition regions. Conversely, a high-resolution discretization (figures 9*c*,*d*) identifies more independent communities, providing detailed information about the transition regions.

Although higher resolutions may lead to a more discerning subdivision of stable, transition and precursor communities, the overall flow structures within these sub-communities remain consistent. If one can reliably identify the main flow structures and associate the sub-communities with stable, transition or precursor states, then the full model would still be effective. For clarity and conciseness, we have chosen an intermediate resolution of 25 boxes in this work; this resolution allows us to distinguish the stable,

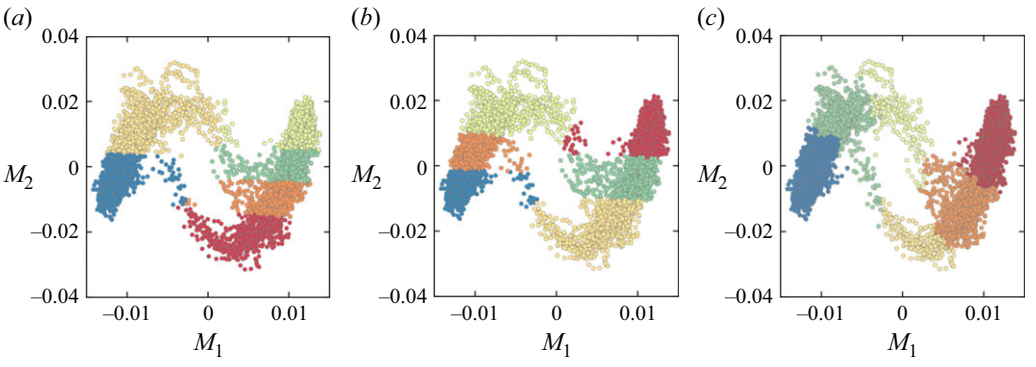

Figure 10. The results of clustering of the (M_1, M_2) phase space using (a,b) the K-means algorithm with different random initializations of the centroids, and (c) our method.

precursor and transition regions, without introducing redundant information from too many clusters.

Appendix C. Comparison with the K-means clustering method

The K-means clustering method is an unsupervised machine learning algorithm, which is widely used to group unlabelled datasets into different clusters (Brunton & Kutz 2022). It has also been applied in previous studies of fluid flows (Kaiser *et al.* 2014; Castillo-Castellanos *et al.* 2019; Fernex *et al.* 2021; Hou *et al.* 2024). In this appendix, we include a comparison of our method to K-means clustering for the phase space of our reversal dynamics, shown in figure 10.

The results confirm the sensitivity of the K-means algorithm to the random initialization of the centroids (see figures 10*a*,*b*), combined with a convergence towards a local minimum. Even in the case when the K-means algorithm produces acceptable and symmetric results (figure 10*b*), an obvious mixing of stable and transition communities persists. This shortcoming emerges since the K-means algorithm takes into account only the spatial distribution of data points, ignoring directional information in the network's connectivity pattern.

Appendix D. Comparison with a simple threshold-based correction scheme for predicting reversal

In this appendix, we compare the prediction of reversals from our model to predictions from a simple threshold-based approach that uses an arbitrary value of $|L|$. For the threshold-based method, we predict flow reversals based on the condition $(|L(t)| - L_c)(|L(t+1)| - L_c) < 0$, where L_c denotes a threshold for the reversal, combined with the sign of the gradient of $L(t)$. The results of the comparison are presented in figure 11. We observe that the accuracy of the latter method is limited by the presence of natural fluctuations in the $|L|$ curve. These fluctuations often lead to false predictions or missed transitions, especially in cases where $|L|$ exhibits declines that do not correspond to actual reversals. In contrast, our model uses cluster information to effectively filter out most of these fluctuations, enabling it to produce more robust and systematic predictions without the need for additional constraints.

Hence a key advantage of our approach lies in its ability to handle fluctuations without requiring special constraints, which in turn yields a robust and effective framework for

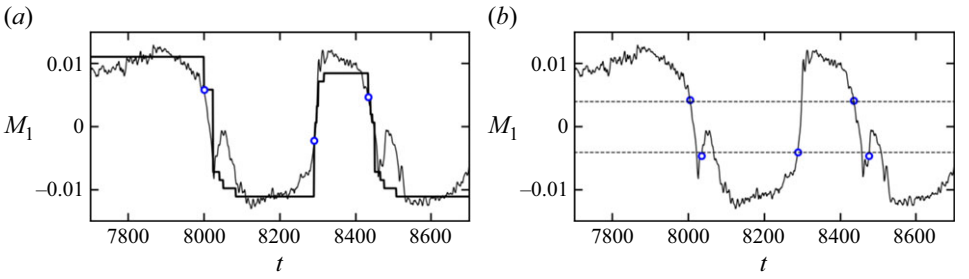

Figure 11. (*a*) The prediction of reversals based on our cluster-based method. The blue points represent the predicted reversal locations. (*b*) The prediction of the reversal based on the simple threshold-based method. The blue points represent the predicted reversal locations. The dashed lines show the value of the threshold, which we adjusted to a value similar to that in our model.

reversal prediction. Despite this advantage, it remains challenging to achieve accurate predictions in the earlier states due to the chaotic nature of the system. We acknowledge this limitation, and plan to investigate further improvements in this direction.

References

Ahlers, G., Grossmann, S. & Lohse, D. 2009 Heat transfer and large scale dynamics in turbulent Rayleigh–Bénard convection. *Rev. Mod. Phys.* **81** (2), 503–537.

Araujo, F.F., Grossmann, S. & Lohse, D. 2005 Wind reversals in turbulent Rayleigh–Bénard convection. *Phys. Rev. Lett.* **95** (8), 084502.

Avila, M., Barkley, D. & Hof, B. 2023 Transition to turbulence in pipe flow. *Annu. Rev. Fluid Mech.* **55** (1), 575–602.

Blass, A., Zhu, X., Verzicco, R., Lohse, D. & Stevens, R.J. 2020 Flow organization and heat transfer in turbulent wall sheared thermal convection. *J. Fluid Mech.* **897**, A22.

Borrero-Echeverry, D., Schatz, M.F. & Tagg, R. 2010 Transient turbulence in Taylor–Couette flow. *Phys. Rev.* E **81** (2), 025301.

Brown, E. & Ahlers, G. 2007 Large-scale circulation model for turbulent Rayleigh–Bénard convection. *Phys. Rev. Lett.* **98** (13), 134501.

Brown, E. & Ahlers, G. 2008 A model of diffusion in a potential well for the dynamics of the large-scale circulation in turbulent Rayleigh–Bénard convection. *Phys. Fluids* **20** (7), 075101.

Brunton, S.L. & Kutz, J.N. 2022 *Data-Driven Science and Engineering: Machine Learning, Dynamical Systems, and Control*. Cambridge University Press.

Brunton, S.L., Noack, B.R. & Koumoutsakos, P. 2020 Machine learning for fluid mechanics. *Annu. Rev. Fluid Mech.* **52** (1), 477–508.

Brunton, S.L., Proctor, J.L. & Kutz, J.N. 2016 Discovering governing equations from data by sparse identification of nonlinear dynamical systems. *Proc. Natl. Acad. Sci.* **113** (15), 3932–3937.

Cai, W. *et al.* 2021 Changing El Niño–Southern oscillation in a warming climate. *Nat. Rev. Earth Environ.* **2** (9), 628–644.

Castillo-Castellanos, A., Sergent, A., Podvin, B. & Rossi, M. 2019 Cessation and reversals of large-scale structures in square Rayleigh–Bénard cells. *J. Fluid Mech.* **877**, 922–954.

Chandra, M. & Verma, M.K. 2011 Dynamics and symmetries of flow reversals in turbulent convection. *Phys. Rev.* E **83** (6), 067303.

Chandra, M. & Verma, M.K. 2013 Flow reversals in turbulent convection via vortex reconnections. *Phys. Rev. Lett.* **110** (11), 114503.

Chartrand, G. & Zhang, P. 2013 *A First Course in Graph Theory*. Courier Corporation.

Danon, L., Diaz-Guilera, A., Duch, J. & Arenas, A. 2005 Comparing community structure identification. *J. Stat. Mech. Theor. Exp.* **2005** (9), P09008.

Deng, N., Noack, B.R., Morzyński, M. & Pastur, L.R. 2022 Cluster-based hierarchical network model of the fluidic pinball–cartographing transient and post-transient, multi-frequency, multi-attractor behaviour. *J. Fluid Mech.* **934**, A24.

Du, Y., Calzavarini, E. & Sun, C. 2024 The physics of freezing and melting in the presence of flows. *Nat. Rev. Phys.* **6** (11), 676–690.

FARAZMAND, M. & SAPSIS, T.P. 2017 A variational approach to probing extreme events in turbulent dynamical systems. *Sci. Adv.* **3** (9), e1701533.
FERNEX, D., NOACK, B.R. & SEMAAN, R. 2021 Cluster-based network modeling – from snapshots to complex dynamical systems. *Sci. Adv.* **7** (25) eabf5006.
GAYOUT, A., BOURGOIN, M. & PLIHON, N. 2021 Rare event-triggered transitions in aerodynamic bifurcation. *Phys. Rev. Lett.* **126** (10), 104501.
GIANNAKIS, D., KOLCHINSKAYA, A., KRASNOV, D. & SCHUMACHER, J. 2018 Koopman analysis of the long-term evolution in a turbulent convection cell. *J. Fluid Mech.* **847**, 735–767.
GIORGINI, L.T., SOUZA, A.N. & SCHMID, P.J. 2024 Reduced Markovian models of dynamical systems. *Phys. D: Nonlinear Phenom.* **470**, 134393.
GLATZMAIER, G.A., COE, R.S., HONGRE, L. & ROBERTS, P.H. 1999 The role of the Earth's mantle in controlling the frequency of geomagnetic reversals. *Nature* **401** (6756), 885–890.
GUO, X.-L., WU, J.-Z., WANG, B.-F., ZHOU, Q. & CHONG, K.L. 2023 Flow structure transition in thermal vibrational convection. *J. Fluid Mech.* **974**, A29.
HADJIGHASEM, A., KARRASCH, D., TERAMOTO, H. & HALLER, G. 2016 Spectral-clustering approach to Lagrangian vortex detection. *Phys. Rev.* E **93** (6), 063107.
VON HARDENBERG, J., GOLUSKIN, D., PROVENZALE, A. & SPIEGEL, E.A. 2015 Generation of large-scale winds in horizontally anisotropic convection. *Phys. Rev. Lett.* **115** (13), 134501.
HOLMES, P. 2012 *Turbulence, Coherent Structures, Dynamical Systems and Symmetry*. Cambridge University Press.
HOU, C., DENG, N. & NOACK, B.R. 2024 Dynamics-augmented cluster-based network model. *J. Fluid Mech.* **988**, A48.
JIMÉNEZ, J. 2023 A Perron–Frobenius analysis of wall-bounded turbulence. *J. Fluid Mech.* **968**, A10.
JIMÉNEZ, J. & MOIN, P. 1991 The minimal flow unit in near-wall turbulence. *J. Fluid Mech.* **225**, 213–240.
KAISER, E. *et al.* 2014 Cluster-based reduced-order modelling of a mixing layer. *J. Fluid Mech.* **754**, 365–414.
KOU, J., LE CLAINCHE, S. & ZHANG, W. 2018 A reduced-order model for compressible flows with buffeting condition using higher order dynamic mode decomposition with a mode selection criterion. *Phys. Fluids* **30** (1), 109–129.
KOU, J. & ZHANG, W. 2017 An improved criterion to select dominant modes from dynamic mode decomposition. *Eur. J. Mech. B/Fluids* **62**, 109–129.
KUTZ, J.N., BRUNTON, S.L., BRUNTON, B.W. & PROCTOR, J.L. 2016 *Dynamic Mode Decomposition: Data-Driven Modeling of Complex Systems*. SIAM.
LASOTA, A. & MACKEY, M.C. 2013 *Chaos, Fractals, and Noise: Stochastic Aspects of Dynamics*, vol. 97 of Applied Mathematical Sciences, 2nd edn. Springer-Verlag.
LEICHT, E.A. & NEWMAN, M.E.J. 2008 Community structure in directed networks. *Phys. Rev. Lett.* **100** (11), 118703.
LI, T.-Y. 1976 Finite approximation for the Frobenius–Perron operator. A solution to Ulam's conjecture. *J. Approx. Theory* **17** (2), 177–186.
LI, X.-M., HE, J.-D., TIAN, Y., HAO, P. & HUANG, S.-D. 2021 Effects of Prandtl number in quasi-two-dimensional Rayleigh–Bénard convection. *J. Fluid Mech.* **915**, A60.
LOHSE, D. & SHISHKINA, O. 2024 Ultimate Rayleigh–Bénard turbulence. *Rev. Mod. Phys.* **96** (3), 035001.
LOHSE, D. & XIA, K.-Q. 2010 Small-scale properties of turbulent Rayleigh–Bénard convection. *Annu. Rev. Fluid Mech.* **42** (1), 335–364.
LUCARINI, V. *et al.* 2016 *Extremes and Recurrence in Dynamical Systems*. John Wiley & Sons.
LUMEY, J.L. 2012 *Stochastic Tools in Turbulence*. Elsevier.
MAITY, P., BITTRACHER, A., KOLTAI, P. & SCHUMACHER, J. 2023 Collective variables between large-scale states in turbulent convection. *Phys. Rev. Res.* **5** (3), 033061.
MAITY, P., KOLTAI, P. & SCHUMACHER, J. 2022 Large-scale flow in a cubic Rayleigh–Bénard cell: long-term turbulence statistics and Markovianity of macrostate transitions. *Phil. Trans. R. Soc. A: Math. Phys. Engng Sci.* **380** (2225), 20210042.
MEZIĆ, I. 2013 Analysis of fluid flows via spectral properties of the Koopman operator. *Annu. Rev. Fluid Mech.* **45** (1), 357–378.
NEWMAN, M.E. 2006 Modularity and community structure in networks. *Proc. Natl Acad. Sci. USA* **103** (23), 8577–8582.
NUNES, F. & NORRIS, R.D. 2006 Abrupt reversal in ocean overturning during the Palaeocene/Eocene warm period. *Nature* **439** (7072), 60–63.
PODVIN, B. & SERGENT, A. 2012 Proper orthogonal decomposition investigation of turbulent Rayleigh–Bénard convection in a rectangular cavity. *Phys. Fluids* **24** (10), 105106.

PODVIN, B. & SERGENT, A. 2015 A large-scale investigation of wind reversal in a square Rayleigh–Bénard cell. *J. Fluid Mech.* **766**, 172–201.
PODVIN, B. & SERGENT, A. 2017 Precursor for wind reversal in a square Rayleigh–Bénard cell. *Phys. Rev.* E **95** (1), 013112.
SCHIKARSKI, T., TRZENSCHIOK, H., PEUKERT, W. & AVILA, M. 2019 Inflow boundary conditions determine T-mixer efficiency. *React. Chem. Engng* **4** (3), 559–568.
SCHMID, P.J. 2010 Dynamic mode decomposition of numerical and experimental data. *J. Fluid Mech.* **656**, 5–28.
SCHMID, P.J. 2022 Dynamic mode decomposition and its variants. *Annu. Rev. Fluid Mech.* **54** (1), 225–254.
SCHMID, P.J., SCHMIDT, O.T., TOWNE, A. & HACK, M.J.P. 2018 Analysis and prediction of rare events in turbulent flows. In *Proceedings of the Summer Program*, Center for Turbulence Research.
SHISHKINA, O. 2021 Rayleigh–Bénard convection: the container shape matters. *Phys. Rev. Fluids* **6** (9), 090502.
SOUCASSE, L., PODVIN, B., RIVIÈRE, P. & SOUFIANI, A. 2019 Proper orthogonal decomposition analysis and modelling of large-scale flow reorientations in a cubic Rayleigh–Bénard cell. *J. Fluid Mech.* **881**, 23–50.
SUGIYAMA, K., *et al.* 2010 Flow reversals in thermally driven turbulence. *Phys. Rev. Lett.* **105** (3), 034503.
SURI, B. 2024 Predictive framework for flow reversals and excursions in turbulence. *Phys. Rev. Lett.* **133** (15), 154002.
DE LA TORRE, A. & BURGUETE, J. 2007 Slow dynamics in a turbulent von Kármán swirling flow. *Phys. Rev. Lett.* **99** (5), 054101.
ULAM, S.M. 1960 *A Collection of Mathematical Problems*. Interscience Publishers.
VELA-MARTÍN, A. & AVILA, M. 2024 Large-scale patterns set the predictability limit of extreme events in Kolmogorov flow. *J. Fluid Mech.* **986**, A2.
VERZICCO, R. & ORLANDI, P. 1996 A finite-difference scheme for three-dimensional incompressible flows in cylindrical coordinates. *J. Comput. Phys.* **123** (2), 402–414.
VLACHAS, P.R., BYEON, W., WAN, Z.Y., SAPSIS, T.P. & KOUMOUTSAKOS, P. 2018 Data-driven forecasting of high-dimensional chaotic systems with long short-term memory networks. *Proc. R. Soc. Lond. A: Math. Phys. Engng Sci.* **474** (2213), 20170844.
WANG, B.-F., ZHOU, Q. & SUN, C. 2020 Vibration-induced boundary-layer destabilization achieves massive heat-transport enhancement. *Sci. Adv.* **6** (21), eaaz8239.
WANG, Y., LAI, P.-Y., SONG, H. & TONG, P. 2018 Mechanism of large-scale flow reversals in turbulent thermal convection. *Sci. Adv.* **4** (11), eaat7480.
XI, H.-D. & XIA, K.-Q. 2007 Cessations and reversals of the large-scale circulation in turbulent thermal convection. *Phys. Rev.* E **75** (6), 066307.
XU, A., CHEN, X. & XI, H.-D. 2021 Tristable flow states and reversal of the large-scale circulation in two-dimensional circular convection cells. *J. Fluid Mech.* **910**, A33.
YANG, R., CHONG, K.L., WANG, Q., VERZICCO, R., SHISHKINA, O. & LOHSE, D. 2020 Periodically modulated thermal convection. *Phys. Rev. Lett.* **125** (15), 154502.
YANG, R., HOWLAND, C.J., LIU, H.-R., VERZICCO, R. & LOHSE, D. 2023 Bistability in radiatively heated melt ponds. *Phys. Rev. Lett.* **131** (23), 234002.
YANG, R., ZHANG, X., REITER, P., LOHSE, D., SHISHKINA, O. & LINKMANN, M. 2022 Data-driven identification of the spatiotemporal structure of turbulent flows by streaming dynamic mode decomposition. *GAMM-Mitteilungen* **45** (1), e202200003.
YANG, Y., VERZICCO, R. & LOHSE, D. 2016 From convection rolls to finger convection in double-diffusive turbulence. *Proc. Natl. Acad. Sci. USA* **113** (1), 69–73.
ZHANG, S., XIA, Z., ZHOU, Q. & CHEN, S. 2020 Controlling flow reversal in two-dimensional Rayleigh–Bénard convection. *J. Fluid Mech.* **891**, R4.
ZHAO, C.-B., WANG, B.-F., WU, J.-Z., CHONG, K.L. & ZHOU, Q. 2022 Suppression of flow reversals via manipulating corner rolls in plane Rayleigh–Bénard convection. *J. Fluid Mech.* **946**, A44.
ZHAO, H.-B., ZHAO, C.-B., ZHOU, Q. & CHONG, K.L. 2024 Thermal convection modulated by actively oscillating filament: the effect of filament rigidity. *Intl J. Heat Mass Transfer* **228**, 125649.
ZIMMERMAN, D.S., TRIANA, S.A. & LATHROP, D.P. 2011 Bi-stability in turbulent, rotating spherical Couette flow. *Phys. Fluids* **23** (6), 065104.